ARTICLE

doi:10.1038/nature21035

Force interacts with macromolecular structure in activation of TGF-β

Xianchi Dong[1]*, Bo Zhao[1]*, Roxana E. Iacob[2], Jianghai Zhu[1], Adem C. Koksal[1], Chafen Lu[1], John R. Engen[2] & Timothy A. Springer[1]

Integrins are adhesion receptors that transmit force across the plasma membrane between extracellular ligands and the actin cytoskeleton. In activation of the transforming growth factor-β1 precursor (pro-TGF-β1), integrins bind to the prodomain, apply force, and release the TGF-β growth factor. However, we know little about how integrins bind macromolecular ligands in the extracellular matrix or transmit force to them. Here we show how integrin $\alpha_V\beta_6$ binds pro-TGF-β1 in an orientation biologically relevant for force-dependent release of TGF-β from latency. The conformation of the prodomain integrin-binding motif differs in the presence and absence of integrin binding; differences extend well outside the interface and illustrate how integrins can remodel extracellular matrix. Remodelled residues outside the interface stabilize the integrin-bound conformation, adopt a conformation similar to earlier-evolving family members, and show how macromolecular components outside the binding motif contribute to integrin recognition. Regions in and outside the highly interdigitated interface stabilize a specific integrin/pro-TGF-β orientation that defines the pathway through these macromolecules which actin-cytoskeleton-generated tensile force takes when applied through the integrin β-subunit. Simulations of force-dependent activation of TGF-β demonstrate evolutionary specializations for force application through the TGF-β prodomain and through the β- and not α-subunit of the integrin.

The three transforming growth factor-β isoforms (TGF-β1–3) and their 30 family relatives in mammals are pivotal in development, wound healing, immune response, and tumorigenesis[1]. Pro-TGF-β1 monomers contain an amino (N)-terminal 249-residue prodomain separated by a pro-protein convertase cleavage site from a carboxy (C)-terminal 112-residue growth factor domain. During biosynthesis, pro-TGF-β dimerizes and disulfide links to latent TGF-β binding proteins (LTBPs) or glycoprotein-A repetitions predominant protein (GARP) in large latent complexes[2]. Each prodomain has an arm domain and straitjacket that form a ring around the growth factor and keep it latent[3]. Binding of integrins $\alpha_V\beta_6$ and $\alpha_V\beta_8$ to RGDLXX(I/L) motifs in the arm domains of pro-TGF-β1 and -β3 (ref. 4) is required for TGF-β activation *in vivo*; however, integrin binding alone is not sufficient for growth factor release[3,5]. Cell biological experiments suggest that traction force exerted by integrin $\alpha_V\beta_6$ on pro-TGF-β1 is required for activation, because activation is abolished by truncation of the β_6-subunit cytoplasmic domain that links to the actin cytoskeleton or by deletion of links between the prodomain and the extracellular environment required for tensile force exertion across the prodomain[5]. In a wider context, how integrins bind and transmit force to macromolecular ligands is important for understanding the assembly and remodelling of extracellular matrices: for example, assembly of fibronectin into the extracellular matrix requires integrin $\alpha_5\beta_1$ and traction force[6].

We have no atomic structures that enable us to understand how integrins bind extracellular matrix macromolecules and transmit force to them. Structures show how small molecules and Arg-Gly-Asp (RGD) peptides bind to integrins, including a pro-TGF-β3 peptide bound to integrin $\alpha_V\beta_6$ (refs 4, 7–9), or reveal interactions with similar peptides in larger, soaked-in fragments constrained by pre-existing integrin crystal lattice[10]. As the effect of force on domains or multi-domain assemblies is highly dependent on the direction of the force vector[11], physiological orientation between integrins and their macromolecular ligands is necessary to understand the biological consequences of force transmission. Here, a co-crystal structure of the integrin $\alpha_V\beta_6$ head bound to intact pro-TGF-β1 provides insights into interaction between integrins and their macromolecular ligands.

Pro-TGF-β1 in complex with integrin $\alpha_V\beta_6$ head

We solved crystal structures of a three-domain $\alpha_V\beta_6$ head fragment containing the α_V β-propeller and thigh domains and β_6 βI domain (2.2 Å) and a 1:2 complex of $\alpha_V\beta_6$ head bound to one monomer of the pro-TGF-β1 dimer (3.5 Å) (Extended Data Table 1 and Fig. 1a). The unbound and pro-TGF-β-bound $\alpha_V\beta_6$ heads crystallize with their βI domains closed and open, respectively (Fig. 1b and Extended Data Fig. 1a). Movements of 3–6 Å in the βI domain transmit allostery from the β1–α1 loop and metal-ion-dependent adhesion site (MIDAS) metal ion that bind the RGD Asp side chain of pro-TGF-β to the α7-helix, which pistons towards the hybrid domain (Fig. 1b and schematized in Fig. 1d, e). The only previous integrin with open crystal structures, $\alpha_{IIb}\beta_3$, shows very similar movements (Extended Data Fig. 1b, c)[7], suggesting sharing of key events in headpiece opening by most integrin β-subunits. Binding of larger integrin $\alpha_V\beta_6$ fragments to pro-TGF-β shows in electron microscopy swing of the β-subunit hybrid domain away from the α-subunit (Fig. 1f–h and Extended Data Fig. 1e)[3]. Because the βI domain is inserted in the hybrid domain, pistoning at one connection at the α7-helix (arrow, Fig. 1b) forces the hybrid domain to pivot at its second connection (Fig. 1d, e). Integrin headpiece opening, communicated by movements within the βI domain between its ligand binding site and hybrid domain interface, increases affinity for ligand[7]. Moreover, opening alters the orientation of the hybrid domain in the upper β-leg, and hence the direction in which force is transmitted when traction force is exerted on the β-subunit by the actin cytoskeleton (Fig. 1d, e).

Integrin binding stabilizes remarkable reshaping of 27 residues in the bowtie tail of the pro-TGF-β arm domain (Figs 1a, 2a, b and Extended Data Fig. 2). The bowtie tail follows bowtie knot cysteines that disulfide-link the two arm domains together (Figs 1a and 2a–c).

[1]Children's Hospital Boston and Department of Biological Chemistry and Molecular Pharmacology, Harvard Medical School, Boston, Massachusetts 02115, USA. [2]Department of Chemistry and Chemical Biology, Northeastern University, Boston, Massachusetts 02115, USA.
*These authors contributed equally to this work.

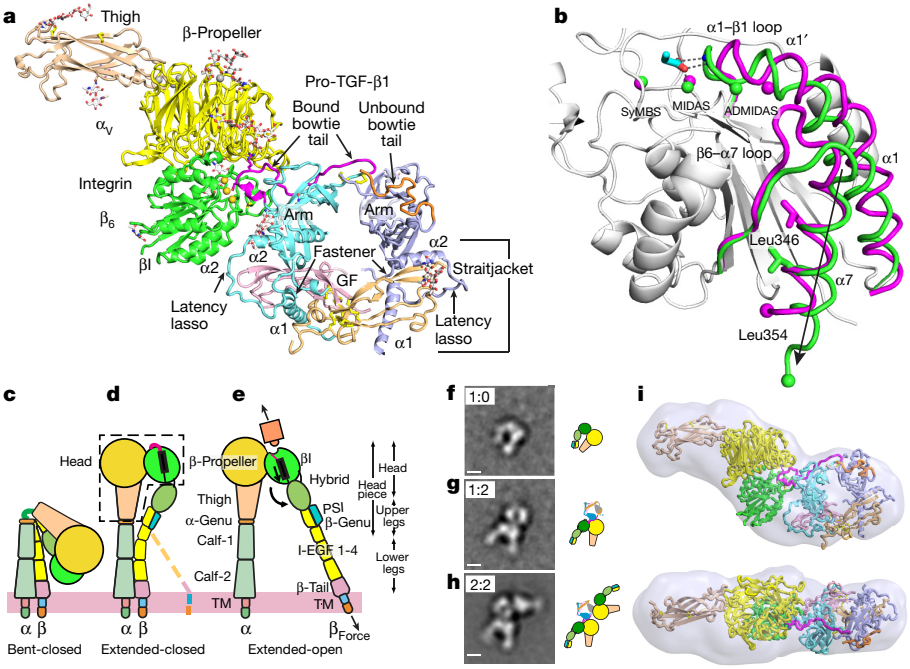

Figure 1 | The $\alpha_V\beta_6$/pro-TGF-β1 complex. **a**, Crystal structure of the 1:2 complex. Ribbon cartoon with domains in different colours, metal ions as gold spheres and bowtie tails in monomers coloured magenta and orange. **b**, Superimposition of $\alpha_V\beta_6$ βI domains with moving regions in magenta (closed) and green (open). Spheres show metal ions and equivalent Cα atoms at end of α7-helix. RGD Asp side chain is shown in cyan with red oxygens and its hydrogen bonds and metal coordination to βI are dashed. SyMBS, synergistic metal ion-binding site; ADMIDAS, adjacent to MIDAS. **c**–**e**, The three major integrin conformational states. TM, transmembrane domain. **f**–**h**, Negative-stain electron micrograph of a $\alpha_V\beta_6$ headpiece/pro-TGF-β1 2:2 complex preparation showing class averages representing 2 isolated $\alpha_V\beta_6$ headpiece (**f**), 7 1:2 complex (**g**), and 35 2:2 complex (**h**) class averages in Extended Data Fig. 1e. Scale bars, 50 Å. **i**, SAXS *ab initio* reconstruction of $\alpha_V\beta_6$ head/pro-TGF-β1 1:2 complex shown as transparent surface with the fit complex crystal structure.

Reshaping includes residues both in and well outside the integrin binding site. Shape shifting occurs in a long hydrophobic groove at the end of the arm jellyroll domain distal from the growth factor (Fig. 2a, b). In the unbound monomer, bowtie tail residues ^{203}-LQVDI-^{207} are disordered and the hydrophobic side chains of Phe210, Leu218, Ala219, and Ile221 bind in the groove. In the integrin-bound conformation, bowtie tail residues move long distances of up to 17 Å. Leu203, Val205, Ile207, and Phe210 replace Phe210, Leu218, Ala219, and Ile221 in the unbound state, respectively (Fig. 2a, b). Residues displaced from the hydrophobic groove contribute to the ^{218}-LATI-^{221} amphipathic α-helix that binds in a hydrophobic pocket formed by the integrin βI domain. Among the residues that move into the hydrophobic groove in the integrin-bound conformation, Val205 and Ile207 take on a β-strand-like conformation and two mainchain hydrogen bonds link this region, which we term the β9′ bridge, to the β3-strand and hence integrate it into the arm domain β-barrel (Fig. 2b).

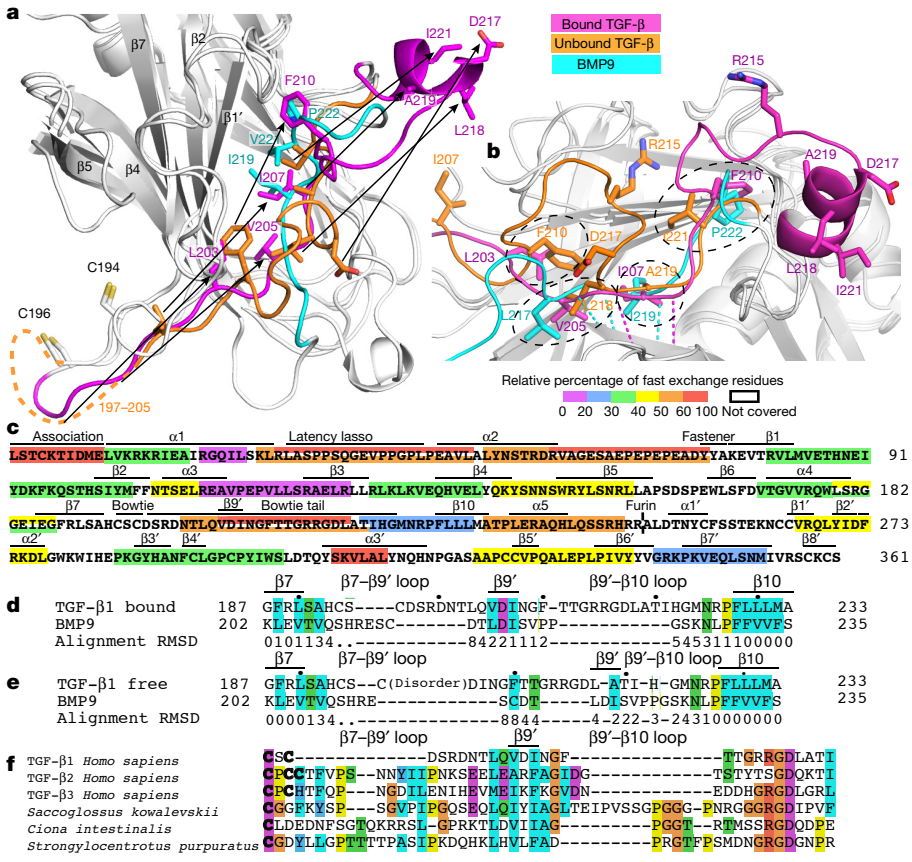

Figure 2 | Reshaping of pro-TGF-β1 by integrin $\alpha_V\beta_6$ and evolution of TGF-β. **a**, **b**, Bowtie tails in pro-TGF-β1 monomers and corresponding residues in BMP9 (ref. 13) after superposition on arm domains. In **b**, β9-strand residue backbone hydrogen bonds are shown as colour-coded dashes. **c**, HDX at 10 s (see key) colour-coded by the percentage of exchangeable residues in single or overlapping peptides. **d**, **e**, Structure-based sequence alignment[18] of arm domains of integrin-bound (**d**) and unbound (**e**) TGF-β1with BMP9 showing β7–β10 region. Black dots mark decadal residues. Cα atom difference from the average position is shown below the alignment in ångströms. **f**, Alignment of TGF-β sequences from human and three representative deuterostomes.

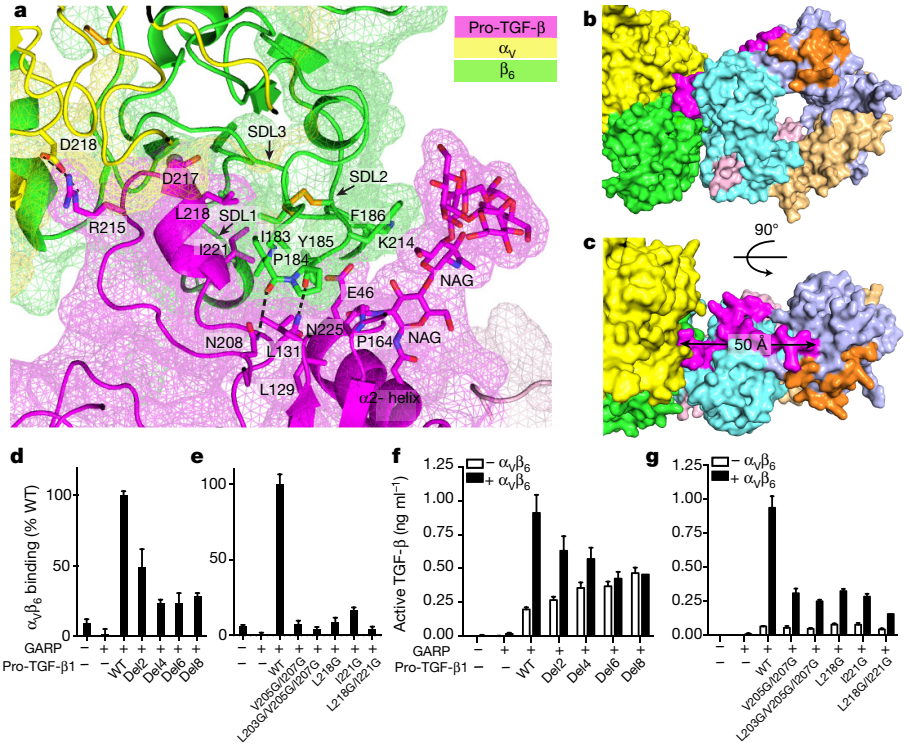

Figure 3 | Interaction between TGF-β1 and $\alpha_V\beta_6$. a, Slab view through the $\alpha_V\beta_6$/TGF-β1 interface showing surfaces of α_V, β_6, and TGF-β1 (mesh), ribbon cartoons, key *N*-glycan and protein side chains (sticks), and hydrogen bonds (black dashes). **b**, **c**, Surface representations of the 1:2 complex, colour coded as in Fig. 1a. **d**–**g**, Binding and activation of wild-type (WT) and mutant pro-TGF-β1 by $\alpha_V\beta_6$. **d**, **e**, Binding of fluorescein isothiocyanate (FITC)-$\alpha_V\beta_6$ to pro-TGF-β1/GARP HEK293T co-transfectants as mean fluorescence intensity. **f**, **g**, Activation of TGF-β1 by HEK293T cells co-transfected with pro-TGF-β1 and GARP, with or without α_V and β_6. Data in **d**–**g** are mean ± s.d. of three biological (transfection) replicates.

To complement crystal structures, we measured backbone dynamics with hydrogen–deuterium exchange mass spectrometry (HDX-MS) (Fig. 2c and Extended Data Figs 3 and 4). Correlating with their large differences in position in the integrin-bound and unbound pro-TGF-β monomers, bowtie tail residues exchange hydrogen for deuterium rapidly (Fig. 2c). In contrast, the remainder of the arm domain shows little change among crystal structures, correlating with slow backbone dynamics (Fig. 2c and Extended Data Figs 3, 4). The jellyroll, β-barrel-like portion of the arm domain with large cross section and extensive β-sheet hydrogen bond network suits it to transmit force with little deformation[12]. In the straitjacket, the α1-helix has slow exchange where it passes between the two growth factor monomers and connects to the fastener, whereas the following latency lasso and the α2-helix at the growth factor/arm domain interface have rapid HDX (Fig. 2c). Prodomain residues 1–9, the 'association region' that contains Cys4 that disulfide links to LTBP or GARP, also undergo rapid HDX and are disordered or differ between monomers (Fig. 2c and Extended Data Fig. 2a).

When the TGF-β and BMP9 (ref. 13) arm domains are structurally aligned by sequence, the integrin-bound state of pro-TGF-β1 aligns best, owing to the change in conformation at the β9′ bridge (Fig. 2d, e). BMPs evolved earlier than TGF-β[1,2]. The sequence that structurally aligns well with the BMP9 β9′-strand in bound pro-TGF-β1, LQVDINGF, is highly conserved among human TGF-β1, -β2, and -β3 and in the single TGF-β present in primitive deuterostomes[1] (Fig. 2f). Thus key specializations in TGF-β, the bowtie disulfides and integrin binding motifs, evolved as insertions in loops on each side of the β9′ bridge (Fig. 2f).

An unusual macromolecular interface

The macromolecular interface is largely formed by three specificity-determining loops (SDL1, 2, and 3) of the βI domain[4] and nearby portions of the α_V β-propeller domain in contact with the protruding bowtie loop of pro-TGF-β1 (Fig. 3a); however, the interface extends further to include the βI domain α2-helix in contact with the prodomain latency lasso (Fig. 1a). The interfaces are much larger than in previous integrin complex structures: 1,090 Å^2 on $\alpha_V\beta_6$ and 1,210 Å^2 on pro-TGF-β. In contrast to the relatively planar surface of most protein–protein complexes, the $\alpha_V\beta_6$ and pro-TGF-β1 interface is highly interdigitated (Figs 1a and 3a). The RGDLATI motif of pro-TGF-β1 protrudes into a deep narrow pocket (approximately 20 Å deep, 15 Å × 15 Å wide) formed at the interface between the α_V β-propeller and β_6 βI domains (Fig. 3a). βI SDL2 forms a complementary protrusion into a deep cleft (approximately 20 Å deep, 20 Å wide) on pro-TGF-β1 between the protruding DLATI α-helix and a glycan *N*-linked to the prodomain α2-helix (Fig. 3a). On the RGDLATI-facing side of SDL2, β_6 Ile183, Tyr185, and the Cys180/Cys187 disulfide together with Ala126 in SDL1 and Ile215 in SDL-3 cradle Leu218 and Ile221 in the RGDLXXI motif. The opposite side of SDL2 together with SDL3 contacts the pro-TGF-β1 α2-helix and the first two *N*-acetylglucosamine residues of its *N*-linked glycan. At its tip, SDL2 forms hydrogen bonds to Asn208 and Asn225 in the bowtie tail (Fig. 3a).

Small-angle X-ray scattering (SAXS) in solution demonstrates a molecular envelope into which the crystal structure fits well (Fig. 1i and Extended Data Fig. 5). The highly constrained and interdigitating interface leads to a well-defined orientation between $\alpha_V\beta_6$ and pro-TGF-β1. In TGF-β1, the specific orientation of the protruding RGDLATI motif is supported by a network of hydrogen bonds that tie it into the arm domain. The DLATI α-helix is followed by the β10-strand that is central in the arm domain, and the intervening four residues are all supported by hydrogen bonds (Extended Data Fig. 6h).

The extensive neoepitope on pro-TGF-β1 created by integrin-induced reshaping includes bowtie tail residues 197–213 that lie outside the integrin footprint and extend 50 Å from the footprint to the bowtie disulfide (Fig. 3b, c). The concept that integrin-induced conformational change in ligands can propagate far outside the integrin binding site may be relevant to integrin remodelling or assembly of the extracellular matrix[6].

Communication across the interface

We predicted that bowtie tail residues that lie outside the binding site are required for other bowtie tail residues to form the integrin binding site. Indeed, serial deletion of bowtie residues encompassing up to residues 199–206 progressively decreased $\alpha_V\beta_6$ binding to pro-TGF-β1 (Fig. 3d) and $\alpha_V\beta_6$-dependent TGF-β1 activation (Fig. 3f) while having no effect on pro-TGF-β1 expression (Extended Data Fig. 6f). Deletion of

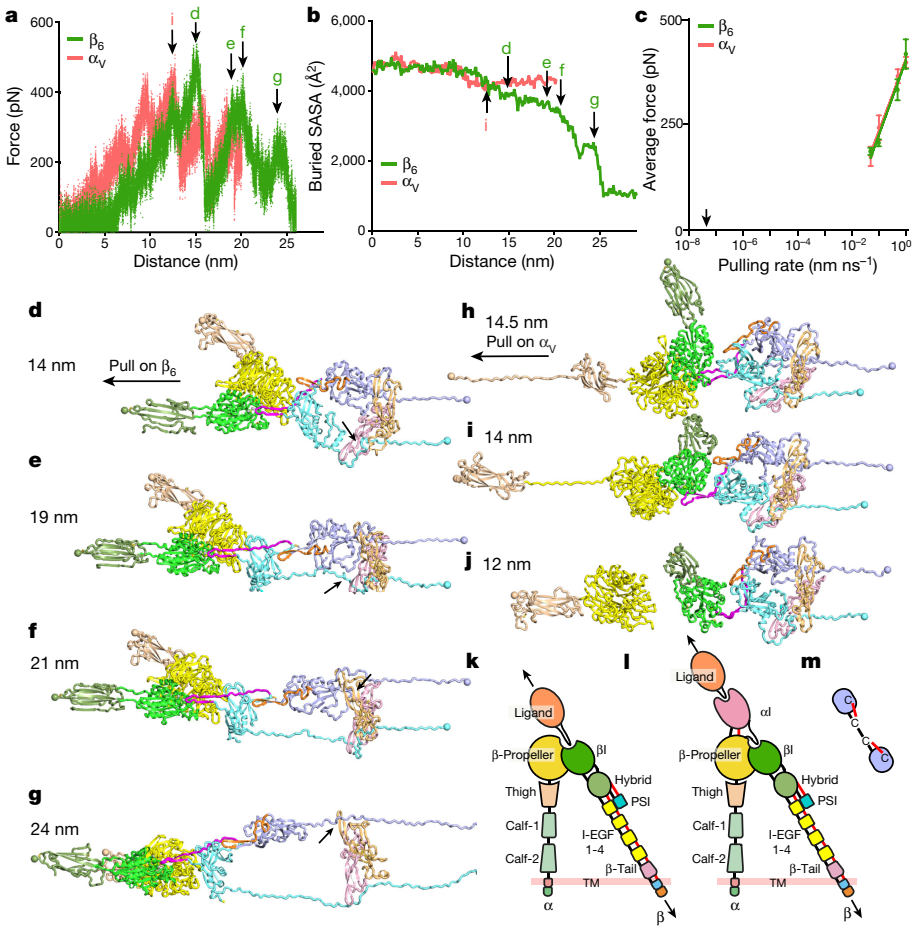

Figure 4 | Simulation of force-dependent activation of pro-TGF-β1 by $\alpha_V\beta_6$. a–j, Using molecular dynamics, pulling at 0.05–1 nm s^{-1} on β_6 hybrid or α_V thigh domain C-terminal residues was resisted by Cys4 residues in each prodomain. **a**, **b**, Force (**a**) and buried solvent-accessible surface area (SASA) between the growth factor and prodomains as a surrogate for release (**b**) for one representative of three simulations at 0.05 nm s^{-1}. Arrows mark events shown in corresponding panels (**d**–**j**). **c**, Average force at each pulling rate (mean ± s.d. of three independent simulations). Arrow marks physiological actin retrograde flow rate. **d**–**j**, Snapshots from pulling on β_6 (**d**–**g**) or α_V (**h**–**j**) at indicated distances. Structures in ribbon cartoon are colour-coded as in Fig. 1a. Spheres show residues used for force application or resistance. Arrows in **d**–**g** mark fastener or α2 helix unfolding. **h**–**j**, Three different simulation results of pulling on α_V. **k**–**m**, Schematics of domain–domain junctions in αI-less integrins such as $\alpha_V\beta_6$ (**k**), αI-containing integrins such as $\alpha_L\beta_2$ (**l**), and detail at integrin EGF domain junctions (**m**). Arrows show tensile force. Domain polypeptide connections and disulfide bonds to junctions are black and red, respectively.

six or eight bowtie tail residues greatly reduced binding and completely abolished activation. Since none of these residues contact $\alpha_V\beta_6$, their deletion demonstrates the requirement of the remarkable reshaping of pro-TGF-β1 for binding and integrin-dependent activation.

Bowtie tail residues L203, V205, and I207 have no contact with the integrin, bury in the hydrophobic groove in the integrin-bound state, and contribute to the β9′ bridge (Fig. 2b–d). Mutations V205G/I207G and L203G/V205G/I207G strongly inhibited integrin binding to and activation of TGF-β (Fig. 3e, g). The importance in binding and activation of residues that lie outside the integrin binding site in stabilizing a particular conformation of the arm domain demonstrates the biological importance of the macromolecular complex defined here. Not only is the binding surface extensive and interdigitated, but regions of the arm domain distal from the ligand binding site contribute to stabilizing a particular integrin-binding conformation of the macromolecule.

Residues L218 and I221 form the hydrophobic face of the DLATI α-helix that projects into the interlocked binding site. Their mutation consistently reduced both binding and integrin-dependent TGF-β activation (Fig. 3e, g). In contrast, single amino-acid substitutions provided no evidence for the importance of integrin contacts with other pro-TGF-β1 residues. Mutations of interacting pro-TGF-β1 residues Glu46, Leu129, Leu131, Pro164, Asn208, or Asn225 have no effect on integrin binding to or activation of TGF-β1 (Extended Data Fig. 6d, e). The importance of the pro-TGF-β1 region covered by these mutations may be to provide overall shape complementarity for the integrin rather than specific interactions.

Together, structure, evolution, mutation, and dynamics provide a view of integrin recognition of a macromolecular extracellular matrix ligand that differs from any previously imagined. Similarity of independent uncomplexed pro-TGF-β1 bowtie tail structures (Extended Data Fig. 2c) suggests that in the conformation that predominates biologically, the integrin-binding motif lies hidden in a hydrophobic groove of the arm domain. Conformational change facilitated by rapid dynamics (Fig. 2c) of this region must precede integrin binding, which sets the stage for subsequent force-dependent activation.

Pathway dependence of activation of TGF-β by force

The highly defined integrin-ligand orientation demonstrated by SAXS, supported by a network of hydrogen bonds that link the RGDLATI motif to the arm domain, define the orientation for force application in TGF-β activation. The force required for release of TGF-β from the $\alpha_V\beta_6$/pro-TGF-β1 complex is applied by actin cytoskeleton movement through adaptors to the β_6-subunit cytoplasmic domain and resisted by LTBP held in the extracellular matrix[5]. Since integrin legs and LTBP have flexible domain–domain interfaces, and will align with force, force in simulations was applied through head-proximal leg domains and resisted by the prodomain Cys4 residues that link to LTBP (Fig. 4a–j). We model TGF-β activation by one integrin, because if two bind, they have opposite orientations (Fig. 1h). Retrograde actin flow stabilizes integrins in the open, high-affinity conformation; thus, if two integrins bind, one will be more aligned with actin flow, and hence more stabilized in a high-affinity, pro-TGF-β-bound state[7,14].

Molecular dynamic simulations of pulling on the integrin β-leg at rates from 1 to 0.05 nm ns^{-1}, each with three independent replicates, gave essentially identical results. Early in simulations, the macromolecular interface rotated into alignment with the pulling direction, and the prodomain association region in each monomer unwound between Cys4 and the position where the α1-helix intercalates between the two growth factor monomers (Fig. 4d and Supplementary Video 1). Thus force applied to one prodomain monomer was transmitted to the other. Pulling on the β_6-subunit was continued until the growth factor was largely released from the prodomain, as shown by decrease in growth factor solvent-accessible surface area burial (Fig. 4b) and disruption of all secondary structure in the straitjacket that surrounds

the growth factor and enforces latency (Fig. 4g). The highest force peaks were associated with unsnapping each fastener and unwinding each α2-helix (Fig. 4a, d–g). The fastener links the end of the α1-helix to the arm domain and encircles the β-finger in each growth factor domain (Fig. 1a)[3]. The prodomain α2-helix interfaces both the arm domain and the growth factor[3,13]. The simulations suggest that these are the most force-resistant elements of the straitjacket, in agreement with findings that securing the fastener with a disulfide abolishes TGF-β activation[3] and that α2-helix mutation in heritable disease is associated with TGF-β activation[3,15]. The force applied in simulations declined with pulling rate (Fig. 4c) and would be lower[16] at the physiological rate of actin retrograde flow (arrow, Fig. 4c).

To better define macromolecular features important in physiological integrin activation by force transmission from the β_6-leg, we compared a non-physiological direction of force application from the α_V-leg. Pulling on α_V caused the macromolecular interface to rotate differently (Fig. 4h–j) from pulling on β_6 (Fig. 4d–g). Although the prodomain α1-helices unwound at their C-terminal ends, little change occurred elsewhere in the prodomain, including the straitjacket (Fig. 4h–j). All 12 α_V simulations had to be terminated after catastrophic failure in the α_V-subunit that precluded TGF-β activation. Either the thigh domain unfolded (Fig. 4h), the β-propeller domain unfolded (Fig. 4i), or the β-propeller domain separated from both pro-TGF-β1 and the β_6-subunit (Fig. 4j).

These comparisons reveal macromolecular specializations in both the integrin and pro-TGF-β for force exertion in a specific, physiological direction. Despite reaching similar levels as in β_6 pulling, force in α_V pulling was completely ineffective in inducing straitjacket removal (Fig. 4a, c and Extended Data Figs 7 and 8). This might relate to the different orientation of the RGD motif between the β9′- and β10-strands after integrin alignment by force, which places more stress on β9′ and the bowtie tail at the R end of RGD in α_V pulling and more stress on β10 at the D end of RGD in β_6 pulling.

The selective unfolding of α_V compared with β_6 by pulling force reveals a feature of integrin domains that has not previously been pointed out as an evolutionary specialization of domains in force transmission pathways. In the cross-section for force transmission, force density is highest at the connection between tandem domains, where there is typically a connection through a single polypeptide chain. In the force-sensitive regions on each side of these junctions, all domains in integrin β-subunits are double-strength, because they have either two polypeptide connections or a single polypeptide connection reinforced with a disulfide bond (Fig. 4k, l). The βI domain is inserted in the hybrid domain, to which it has two polypeptide connections. The hybrid and EGF domains each have disulfide bonds at their connecting ends, with only one residue in between (Fig. 4m). Integrin EGF domains have a specialization for bearing force that sets them apart from classical EGF domains: an extra disulfide between their first and fifth Cys residues (C1 and C5); only one residue intervenes between C8 in one integrin EGF domain and C1 in the next.

In contrast, the connections between the integrin α-subunit domains have a single polypeptide connection and lack securing disulfides (Fig. 4k). The ligand-binding αI domain, present in a subset of integrin α-subunits, relays force and activation to the βI domain[14,17]. In an exception that proves the rule, the αI domain has two polypeptide connections and a disulfide reinforcement (Fig. 4l). The presence of double connections at all domain termini in the force-bearing β-subunit pathway (13/13) and not in the non-force-bearing α-subunit pathway (0/7) in integrins is statistically significant (distribution by chance alone, $P < 10^{-5}$), and strongly suggests that this is a specialization of integrins driven by evolution.

In summary, we have described how an integrin reshapes a macromolecular, extracellular matrix ligand. The binding orientation and the structures of the integrin and its ligand appear to have evolved to support specific pathways for tensile force transmission through each macromolecule to enable cytoskeletal force applied to integrin $\alpha_V\beta_6$ through its β-subunit to activate TGF-β1.

Online Content Methods, along with any additional Extended Data display items and Source Data, are available in the online version of the paper; references unique to these sections appear only in the online paper.

Received 11 January; accepted 6 December 2016.
Published online 25 January 2017.

1. Robertson, I. B. & Rifkin, D. B. Unchaining the beast; insights from structural and evolutionary studies on TGFβ secretion, sequestration, and activation. *Cytokine Growth Factor Rev.* **24,** 355–372 (2013).
2. Hinck, A. P., Mueller, T. D. & Springer, T. A. Structural biology and evolution of the TGF-β family. *Cold Spring Harb. Perspect. Biol.* **8,** a022103 (2016).
3. Shi, M. *et al.* Latent TGF-β structure and activation. *Nature* **474,** 343–349 (2011).
4. Dong, X., Hudson, N. E., Lu, C. & Springer, T. A. Structural determinants of integrin β-subunit specificity for latent TGF-β. *Nature Struct. Mol. Biol.* **21,** 1091–1096 (2014).
5. Robertson, I. B. & Rifkin, D. B. Regulation of the bioavailability of TGF-β and TGF-β-related proteins. *Cold Spring Harb. Perspect. Biol.* **8,** a021907 (2016).
6. Schwarzbauer, J. E. & DeSimone, D. W. Fibronectins, their fibrillogenesis, and *in vivo* functions. *Cold Spring Harb. Perspect. Biol.* **3,** a005041 (2011).
7. Springer, T. A. & Dustin, M. L. Integrin inside-out signaling and the immunological synapse. *Curr. Opin. Cell Biol.* **24,** 107–115 (2012).
8. Nagae, M. *et al.* Crystal structure of $\alpha_5\beta_1$ integrin ectodomain: atomic details of the fibronectin receptor. *J. Cell Biol.* **197,** 131–140 (2012).
9. Xiong, J. P. *et al.* Crystal structure of the extracellular segment of integrin $\alpha_V\beta_3$ in complex with an Arg-Gly-Asp ligand. *Science* **296,** 151–155 (2002).
10. Van Agthoven, J. F. *et al.* Structural basis for pure antagonism of integrin $\alpha_V\beta_3$ by a high-affinity form of fibronectin. *Nature Struct. Mol. Biol.* **21,** 383–388 (2014).
11. Chen, Y., Radford, S. E. & Brockwell, D. J. Force-induced remodelling of proteins and their complexes. *Curr. Opin. Struct. Biol.* **30,** 89–99 (2015).
12. Clarke, J. & Williams, P. M. in *Protein Folding Handbook* Part 1 (eds Buchner, J. & Kiefhaber, T.) 1111–1142 (Wiley-VCH, 2005).
13. Mi, L.-Z. *et al.* Structure of bone morphogenetic protein 9 procomplex. *Proc. Natl Acad. Sci. USA* **112,** 3710–3715 (2015).
14. Nordenfelt, P., Elliott, H. L. & Springer, T. A. Coordinated integrin activation by actin-dependent force during T-cell migration. *Nature Commun.* **7,** 13119 (2016).
15. Janssens, K. *et al.* Camurati-Engelmann disease: review of the clinical, radiological, and molecular data of 24 families and implications for diagnosis and treatment. *J. Med. Genet.* **43,** 1–11 (2006).
16. Evans, E. & Ritchie, K. Strength of a weak bond connecting flexible polymer chains. *Biophys. J.* **76,** 2439–2447 (1999).
17. Sen, M., Yuki, K. & Springer, T. A. An internal ligand-bound, metastable state of a leukocyte integrin, $\alpha_X\beta_2$. *J. Cell Biol.* **203,** 629–642 (2013).
18. Wang, S., Ma, J., Peng, J. & Xu, J. Protein structure alignment beyond spatial proximity. *Sci. Rep.* **3,** 1448 (2013).

Supplementary Information is available in the online version of the paper.

Acknowledgements This work was supported by National Institutes of Health grant R01AR067288, the Charles A. King Trust Postdoctoral Research Fellowship Program, Bank of America, N.A., Co-Trustee, and research collaboration with the Waters Corporation. For crystallography, SAXS, and simulations, we thank GM/CA-CAT beamline 23-ID at the Advanced Photon Source, beamline X9A at the National Synchotron Light Source, and the Pittsburgh Supercomputing Center, respectively.

Author Contributions T.A.S., X.D., and B.Z. designed experiments and wrote the manuscript. B.Z. and X.D. performed biochemical studies and crystallization. X.D. performed data collection and structure determination. X.D. and B.Z. performed molecular dynamics. B.Z. and A.K. performed SAXS. X.D. and J.Z. performed electron microscopy. B.Z., R.E.I., and J.R.E. performed HDX-MS. C.L. aided experiment design and data analysis.

Author Information Reprints and permissions information is available at www.nature.com/reprints. The authors declare no competing financial interests. Readers are welcome to comment on the online version of the paper. Correspondence and requests for materials should be addressed to T.A.S. (timothy.springer@childrens.harvard.edu).

Reviewer Information *Nature* thanks T. Ha, Y. Shan and the other anonymous reviewer(s) for their contribution to the peer review of this work.

METHODS

No statistical methods were used to predetermine sample size. The experiments were not randomized and investigators were not blinded to allocation during experiments and outcome assessment.

Protein expression and purification. The human pro-TGF-β1 construct contains an N-terminal 8-His tag, followed by a SBP tag and a 3C protease site. A C4S mutation, an R249A furin cleavage site mutation and *N*-glycosylation site mutations N107Q and N147Q were introduced to facilitate protein expression, secretion, and crystallization. Pro-TGF-β1 was expressed in CHO Lec 3.2.8.1 cells using the pEF1-puro vector, purified in three steps as described in ref. 3 and yielded 1 mg purified protein per litre of culture supernatant. The same protein was used in electron microscopy, SAXS, HDX, and surface plasmon resonance.

Soluble $\alpha_V\beta_6$ headpiece was prepared as in ref. 4. The $\alpha_V\beta_6$ head used the same α_V construct as in the $\alpha_V\beta_6$ headpiece and the β_6 βI domain (residues 108–352) with I270C mutation followed by a 6× His tag. Proteins expressed in HEK293S Gnt I$^-$ cells with EX-CELL 293 Serum-Free Medium (Sigma) were purified using Ni-NTA affinity column (Qiagen). Protein was cleaved with 3C protease at 4 °C overnight and passed through Ni-NTA resin and further purified using an ion exchange gradient from 50 mM NaCl to 1 M NaCl, 20 mM Tris-HCl, pH 8.0 (Q fast-flow Sepharose, GE Healthcare) and gel filtration (Superdex 200, GE Healthcare). Cell lines were obtained as described previously[3,4] and not authenticated or tested for mycoplasma contamination.

Crystal structures. Crystals of $\alpha_V\beta_6$ head (1 μl, 5 mg/ml in 20 mM Tris-HCl pH 7.4 and 150 mM NaCl) were formed in hanging drops at 20 °C with 1 μl of 5% PEG 3000, 25% PEG 200, 0.1 M MES pH 6.0. Crystals of $\alpha_V\beta_6$ head/pro-TGF-β1 (3 mg/ml, 1:2 stoichiometry, separated from 2:2 complex and uncomplexed material by gel filtration in the same buffer as the head except with 1 mM $MnCl_2$ and 0.2 mM $CaCl_2$) were similarly formed with 9% PEG 8000, 0.1 M imidazole pH 8.0. Crystals were cryo-protected by well solution containing 30% glycerol. Data collection at the wavelength of 1.0332 Å and structure determination were as in ref. 4 with truncated $\alpha_V\beta_6$ headpiece[4] and porcine pro-TGF-β1 (ref. 3) as search models for molecular replacement.

In the $\alpha_V\beta_6$ head model, 96.1%, 3.9%, and 0% of residues had backbone dihedral angles in the favoured, allowed, and outlier regions of the Ramachandran plot, respectively as reported by MolProbity. The MolProbity percentile scores were both 99 for clash and geometry. In the $\alpha_V\beta_6$ head/pro-TGF-β1 complex model, 90.0%, 8.8%, and 0.4% of residues had backbone dihedral angles in the favoured, allowed, and outlier regions of the Ramachandran plot, respectively, as reported by MolProbity. The MolProbity percentile scores were 97 and 100 for clash and geometry, respectively.

SAXS. The $\alpha_V\beta_6$ head/pro-TGF-β1 complex (1:2 stoichiometry) was purified by gel-filtration as described above. Samples at 0.4 and 3 mg/ml concentrations were passed through a 0.22 μm pore Ultrafree-MC Centrifugal Filter (Millipore, Billerica, Massachusetts, USA) before measurement. Measurements at Brookhaven National Laboratories Beamline X9 used a high-sensitivity 300 K Pilatus detector at 3.4 m distance. Exposures (20 s) in triplicate were collected while the protein sample was passed through a flow capillary. All datasets from both concentrations were merged and $I(0)$ and the pair distance distribution function $P(r)$ were calculated from the merged scattering intensities $I(q)$ using the software PRIMUS[19]. *Ab initio* modelling, averaging, and surface map conversion were as in ref. 20.

Negative-stain electron microscopy. Purified pro-TGF-β1 and $\alpha_V\beta_6$ headpiece (2:2 molar ratio) were subjected to Superdex S200 chromatography in HBS (20 mM HEPES pH 7.4, 150 mM NaCl, 1 mM $CaCl_2$, $MgCl_2$) and the peak fraction was subjected to negative-stain electron microscopy as described[3].

Surface plasma resonance. Surface plasmon resonance studies were performed using a Biacore 3000 instrument (GE Healthcare). Pro-TGF-β1, latency associated peptide 1 (LAP1), and endoglycosidase-H-treated pro-TGF-β1 were amine immobilized on a CM5 chip. Purified $\alpha_V\beta_6$ headpiece was injected at 20 μl/min in HBS. The surface was regenerated with a pulse of 25 mM HCl at the end of each cycle. Kinetics were analysed with Biacore evaluation software version 4.0.1 (GE Healthcare).

Pro-TGF-β1 mutagenesis. Wild-type human pro-TGF-β1 was inserted into a pcDNA3.1(−) expression vector. Mutations and serial truncation mutations were generated using QuikChange (Stratagene). All mutations were verified by DNA sequencing.

Pro-TGF-β1 cell surface binding by FACS. Assays were as described[4]. Wild-type or mutant pro-TGF-β1 in pcDNA3.1(−) vector and GARP in pLEXm vector were transiently co-transfected into 293T cells using lipofectamine 2000 (Life Technologies). Specific binding of 50 nM FITC-$\alpha_V\beta_6$ to pro-TGF-β1-GARP on transfectants was expressed as binding in 1 mM Mg^{2+}/Ca^{2+} minus binding in 10 mM EDTA. Cell surface expression of pro-TGF-β1-GARP was determined by flow cytometry using TW7-28G11 anti-TGF-β1 antibody (catalogue number 146704, Biolegend, San Diego, California) and FITC conjugated anti-mouse IgG secondary antibody (F-2761, Thermo Fisher Scientific, Rockford, Illinois). HEK293T cell line from ATCC was not authenticated or tested for mycoplasma contamination.

Pro-TGF-β1 activation. Assays were done similarly as previously described[4]. Pro-TGF-β1/GARP co-transfected 293T cells were co-cultured with human $\alpha_V\beta_6$ or mock 293T transfectants and transformed mink lung cells (TMLC) provided by D. Rifkin transfected with a TGF-β1-sensitive luciferase reporter[21]. Cells were lysed after 24 h of incubation and the luciferase activity induced by TGF-β1 was measured using the luciferase assay system (Promega). A standard curve was calculated with serial diluted purified mature TGF-β1 protein (eBiosciences). The transformed mink lung cell line was verified to be TGF-β-sensitive and was not tested for mycoplasma contamination.

HDX. HDX experiments were performed as described[22]. Sixty-two picomoles of pro-TGF-β1 were diluted 15-fold into 20 mM Tris, 150 mM NaCl, 99% D_2O (pH 8.0) at room temperature. At deuterium exchange time points from 10 s to 180 min, an aliquot was quenched by adjusting the pH to 2.5 with an equal volume of 150 mM potassium phosphate, 0.5 M tris (2-carboxyethyl)phosphine hydrochloride (TCEP-HCl), H_2O. Samples were digested with pepsin and analysed as described[22]. The average amount of back-exchange was 18–25%, based on analysis of highly deuterated peptide standards. All comparison experiments were done under identical experimental conditions such that deuterium levels were not corrected for back-exchange and are therefore reported as relative[23]. All experiments were performed in triplicate. The error of measuring the mass of each peptide was ±0.12 Da. Pro-TGF-β1 sequence coverage was 81.3% corresponding to 60 peptic peptides (Extended Data Figs 3 and 4).

Force-probe molecular dynamics simulations. The β_6 hybrid domain[4] was added to the open $\alpha_V\beta_6$ head in the 2:1 complex by superimposing on the open $\alpha_{IIb}\beta_3$ headpiece[24] and modelling residues at the junction. To minimize the simulation box, thigh or hybrid domains were removed in β_6 and α_V pulling, respectively. The protein was solvated in a ~50 nm × 11 nm × 9 nm rectangular box containing ~600,000 atoms with simple point charge water. Simulations with Gromacs 5.1.2 used OPLS-AA as described[25]. Harmonic springs (500 kJ/mol/nm) were attached to β_6 residue Cys432 or α_V residue Thr596 and moved away from the two prodomain Cys4 residues at 0.05, 0.1, 0.5, or 1 nm/ns for ~30 nm. Cys4 residues were positionally restrained with spring constants of 1,000 kJ/mol/nm. Three repeats at each pulling rate differed in random initial velocities. Simulations were performed using Bridges at the Pittsburgh Supercomputing Center. Average force was calculated from the beginning of pulling until the completion of the last major event arrowed in Extended Data Figs 7a–l and 8a–l. Solvent accessible surface areas were calculated with the get_area command of Pymol.

Data availability. Structural coordinates have been deposited in the Protein Data Bank under accession numbers 5FFG and 5FFO for the $\alpha_V\beta_6$ head and $\alpha_V\beta_6$ head/pro-TGF-β1 1:2 complex, respectively. X-ray diffraction images have been deposited in the SBGrid Data Bank with digital object identifiers http://dx.doi.org/10.15785/SBGRID/391 (the $\alpha_V\beta_6$ head) and http://dx.doi.org/10.15785/SBGRID/392 ($\alpha_V\beta_6$ head/pro-TGF-β1 1:2 complex). The remaining data that support the findings of this study are available from the corresponding author upon reasonable request.

19. Konarev, P. V., Volkov, V. V., Skolova, A. V., Koch, M. H. & Svergun, D. I. PRIMUS: a Windows PC-based system for small-angle scattering data analysis. *J. Appl. Crystallogr.* **36,** 1277–1282 (2003).
20. Eng, E. T., Smagghe, B. J., Walz, T. & Springer, T. A. Intact $\alpha_{IIb}\beta_3$ integrin is extended after activation as measured by solution X-ray scattering and electron microscopy. *J. Biol. Chem.* **286,** 35218–35226 (2011).
21. Abe, M. *et al.* An assay for transforming growth factor-β using cells transfected with a plasminogen activator inhibitor-1 promoter-luciferase construct. *Anal. Biochem.* **216,** 276–284 (1994).
22. Iacob, R. E. B.-A. *et al.* Investigating monoclonal antibody aggregation using a combination of H/DX-MS and other biophysical measurements. *J. Pharm. Sci.* **102,** 4315–4329 (2013).
23. Wales, T. E. & Engen, J. R. Hydrogen exchange mass spectrometry for the analysis of protein dynamics. *Mass Spectrom. Rev.* **25,** 158–170 (2006).
24. Zhu, J., Zhu, J. & Springer, T. A. Complete integrin headpiece opening in eight steps. *J. Cell Biol.* **201,** 1053–1068 (2013).
25. Zhou, M. *et al.* A novel calcium-binding site of von Willebrand factor A2 domain regulates its cleavage by ADAMTS13. *Blood* **117,** 4623–4631 (2011).
26. Svergun, D. I., Barberato, C. & Koch, M. H. J. *CRYSOL* – a program to evaluate X-ray solution scattering of biological macromolecules from atomic coordinates. *J. Appl. Crystallogr.* **28,** 768–773 (1995).

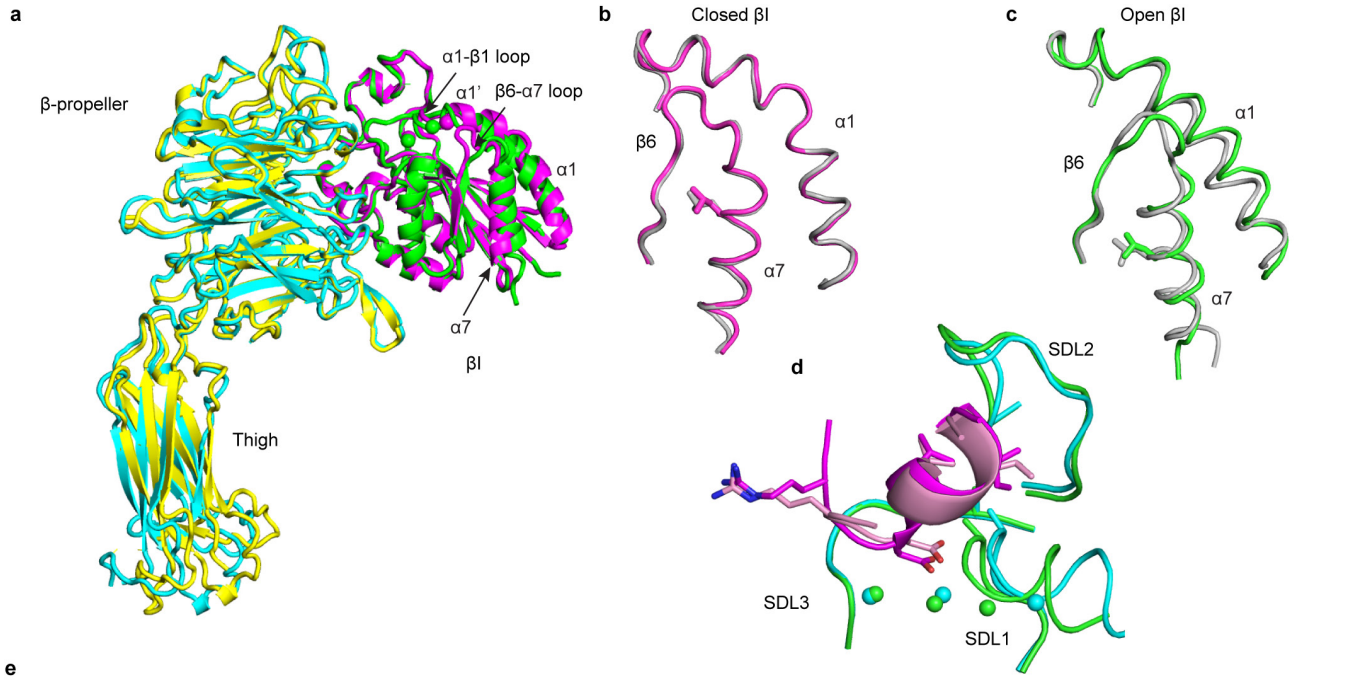

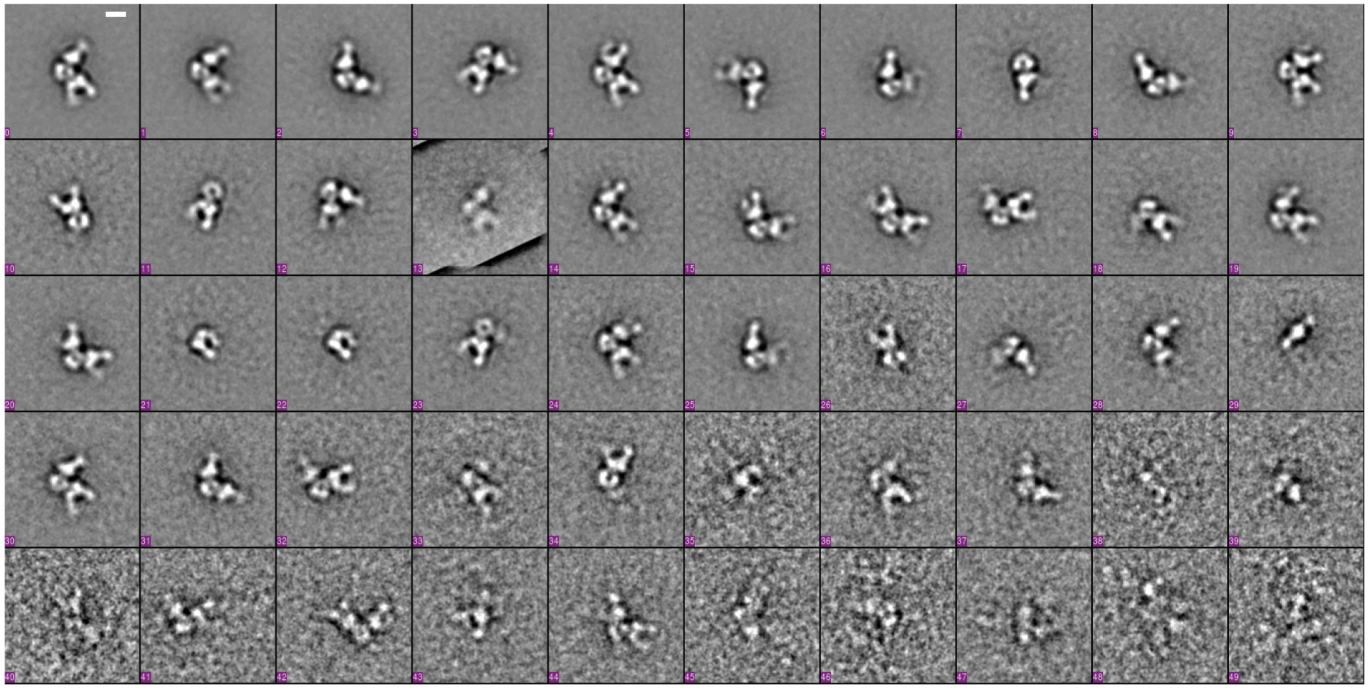

Extended Data Figure 1 | Crystal structure comparisons. **a**, Superimposition of $\alpha_V\beta_6$ headpiece (Protein Data Bank accession number 4UM9, chains A and B)[4] in closed conformation (α_V yellow, β_6 magenta) and head in open conformation in complex with pro-TGF-β1 (α_V cyan, β_6 green). **b**, **c**, Superimposed β_3 and β_6 βI domains, showing only moving regions in magenta or green (β_6) and white (β_3). **d**, Comparison of the macromolecular pro-TGF-β1 complex and soaked-in pro-TGF-β3 peptide complex showing integrin-binding loops (magenta and pink, respectively) and βI domain loops and metal ions (green and cyan, respectively). The conformation of the ^{215}-RGDLATI-^{221} motif in intact pro-TGF-β1 when co-crystallized with $\alpha_V\beta_6$ is similar to that of the ^{241}-RGDLGRL-^{247} motif in a pro-TGF-β3 peptide soaked into $\alpha_V\beta_6$ crystals[4]. **e**, The complete set of electron microscopy class averages (5,546 particles) from a gel filtration peak of the 2:2 pro-TGF-β1/$\alpha_V\beta_6$ complex. While most class averages show 2:2 complexes, 1:2 complexes and isolated $\alpha_V\beta_6$ are also present, presumably because of dissociation of 2:2 complexes. Scale bar in the first-class average is 50 Å.

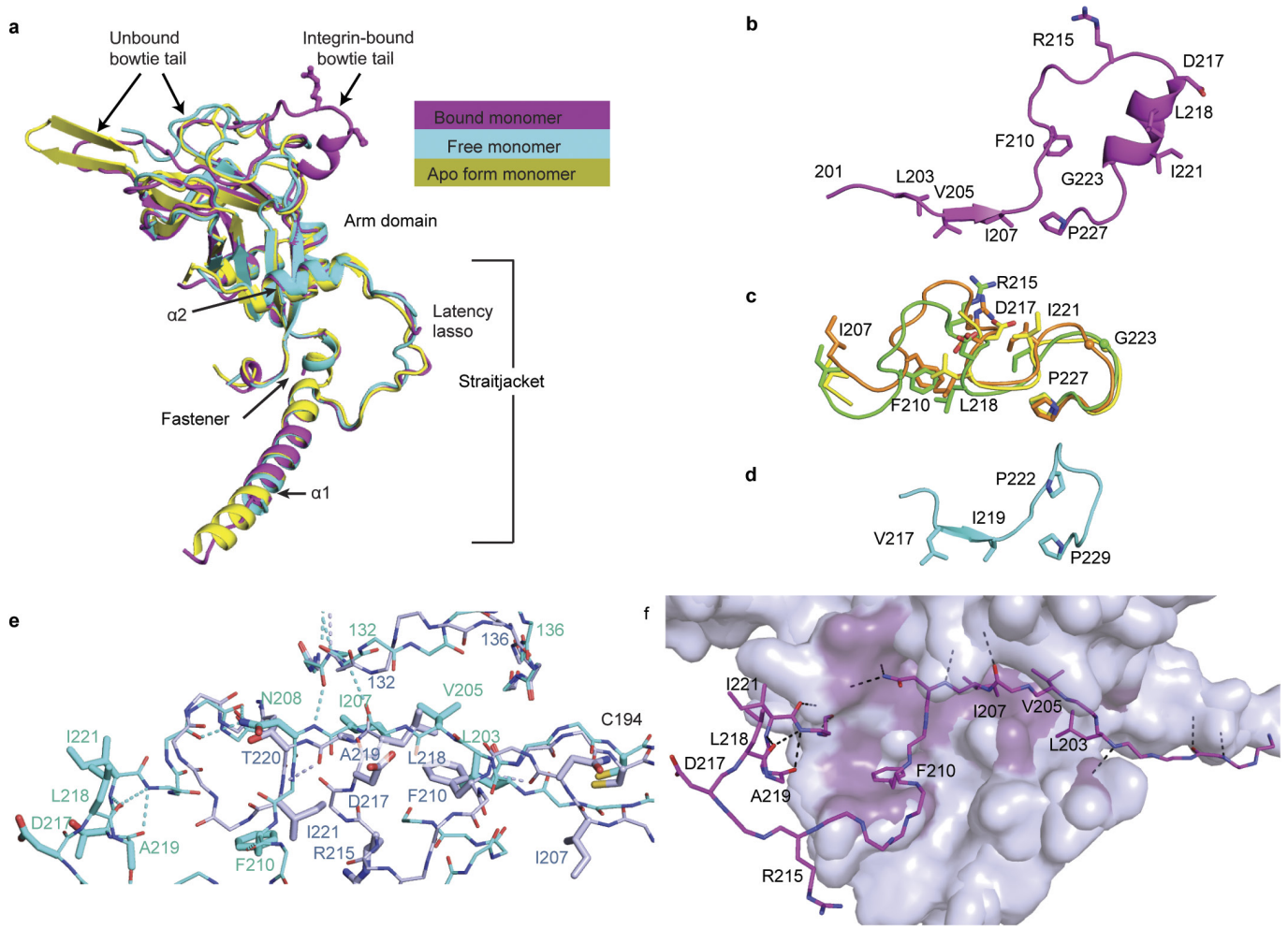

Extended Data Figure 2 | Pro-TGF-β structure comparisons. **a**, Superimposition of bound and free pro-TGF-β1 prodomain monomers from the complex with $\alpha_V\beta_6$ and from an unbound (apo) porcine pro-TGF-β1 dimer[3]. **b–d**, The bowtie tail regions in pro-TGF-β1 crystal structures and the corresponding region of pro-BMP9, shown in identical orientations and vertically aligned after superposition on the arm domain. **b**, Integrin-bound human pro-TGF-β1 monomer. **c**, Bowtie tail regions in unbound monomers from the complex (orange), free human pro-TGF-β1 (B.Z., X.D. and T.A.S., unpublished observations, green), and free porcine pro-TGF-β1 (ref. 3) (yellow). Arg215 and Asp217 of the RGD motif in the unbound form are exposed to solvent but are not sufficiently accessible for integrin binding. **d**, BMP9 (ref. 13). **e**, Integrin-induced bowtie tail reshaping. Bowtie tails in the integrin-bound (cyan) and free (light blue) monomers are shown as backbone in thin stick with side chains participating in hydrogen bonds or interacting with the integrin or arm domain hydrophobic pocket shown as thick sticks. The side chains of residues N208 and T220 form hydrogen bonds to backbone in equivalent positions at a turn. Hydrogen bonds in the integrin-binding region and β9′-bridge region are shown in the same colour as sticks. The backbone shifts at residues 132–136 that line the bowtie groove. **f**, The integrin-bound bowtie tail is stabilized in a hydrophobic cleft of the arm domain. Bowtie tail backbone and side chains of key residues are shown as magenta sticks, and the remainder of the arm domain is shown as a silver surface with regions in close contact with the bowtie coloured violet-purple. Hydrogen bonds are shown as black dashed lines. Altogether, the HDX and analysis of crystal lattice contacts in Extended Data Figs 3 and 4 together with comparisons of monomer structures in Extended Data Fig. 2a–c provide insights into the flexibility of the bowtie tail and association regions. In the absence of integrin binding, the bowtie tail is dynamic. The structure of its C-terminal region is similar in the uncomplexed monomer here and a previous uncomplexed, porcine pro-TGF-β1 dimer (apo form)[3]. However, its N-terminal portion is either unstructured or dependent on crystal lattice contacts. The N-terminal association region is similarly either unstructured or adopts a structure that is dependent on crystal lattice contacts.

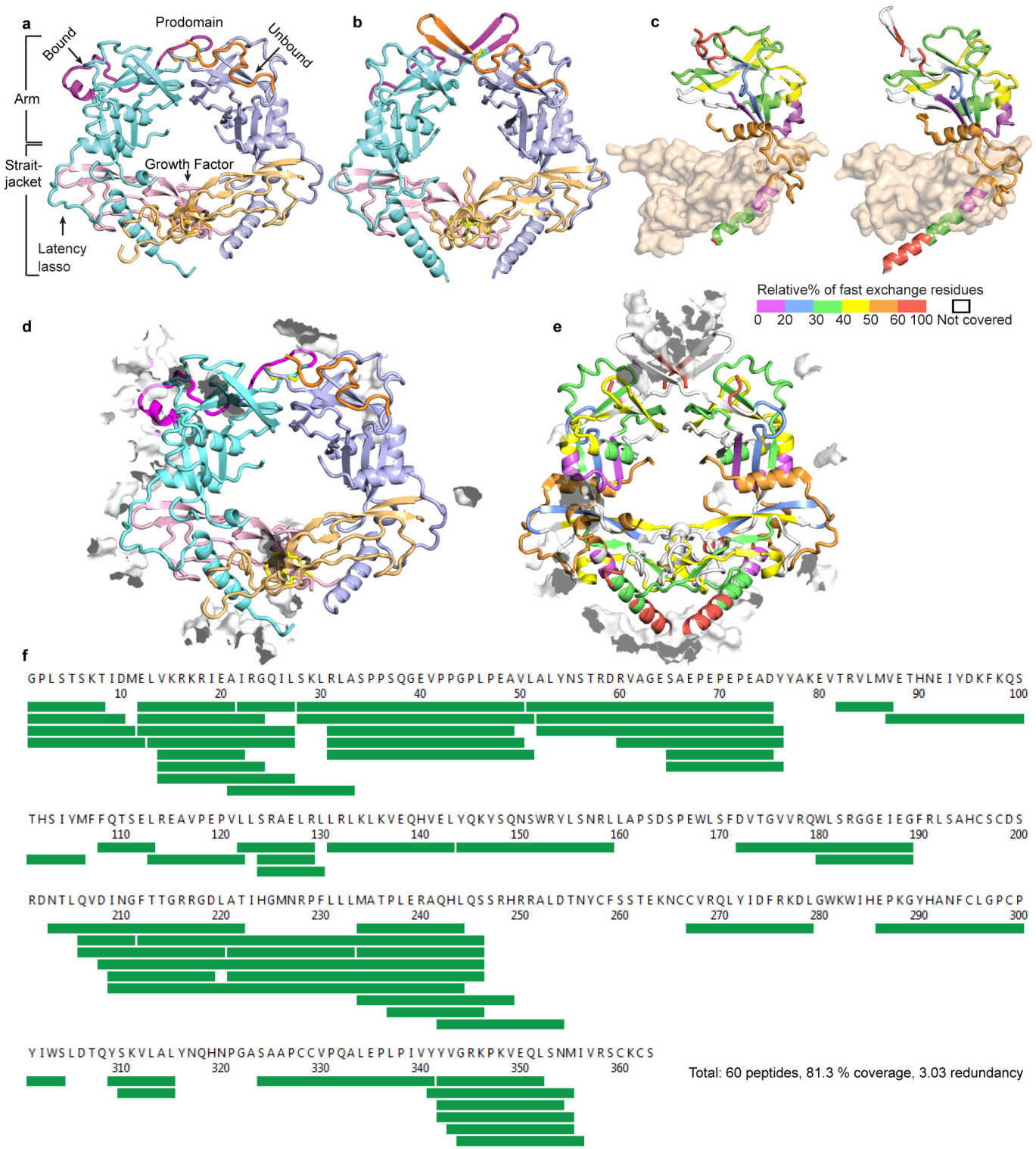

Extended Data Figure 3 | Contacts in crystals of pro-TGF-β1 and HDX. **a**, **b**, The pro-TGF-β1 moiety of the 2:1 complex (**a**) and isolated porcine pro-TGF-β1 (**b**) in identical orientations. Ribbon cartoons are coloured as in Fig. 1a. **c**, Unbound prodomain monomer from the complex structure (left) and prodomain monomer from isolated TGF-β1 (right) shown as ribbon cartoons with growth factor dimers in identical orientations. Ribbon cartoons are coloured according to the relative percentage of HDX at 10 s shown in the key, using peptides shown in Fig. 2a. **d**, **e**, Crystal lattice environments of integrin-bound human pro-TGF-β1 (**d**) and uncomplexed porcine pro-TGF-β1 (**e**). Portions of other molecules in the crystal that pack within 4 Å, including the bound integrin, are shown as white surfaces. Colouring in **d** is as in Fig. 2a and colouring in **e** is as in **c**, according to fast exchange rate as shown in the key. **f**, HDX-MS pepsin peptide coverage map of human pro-TGF-β1.

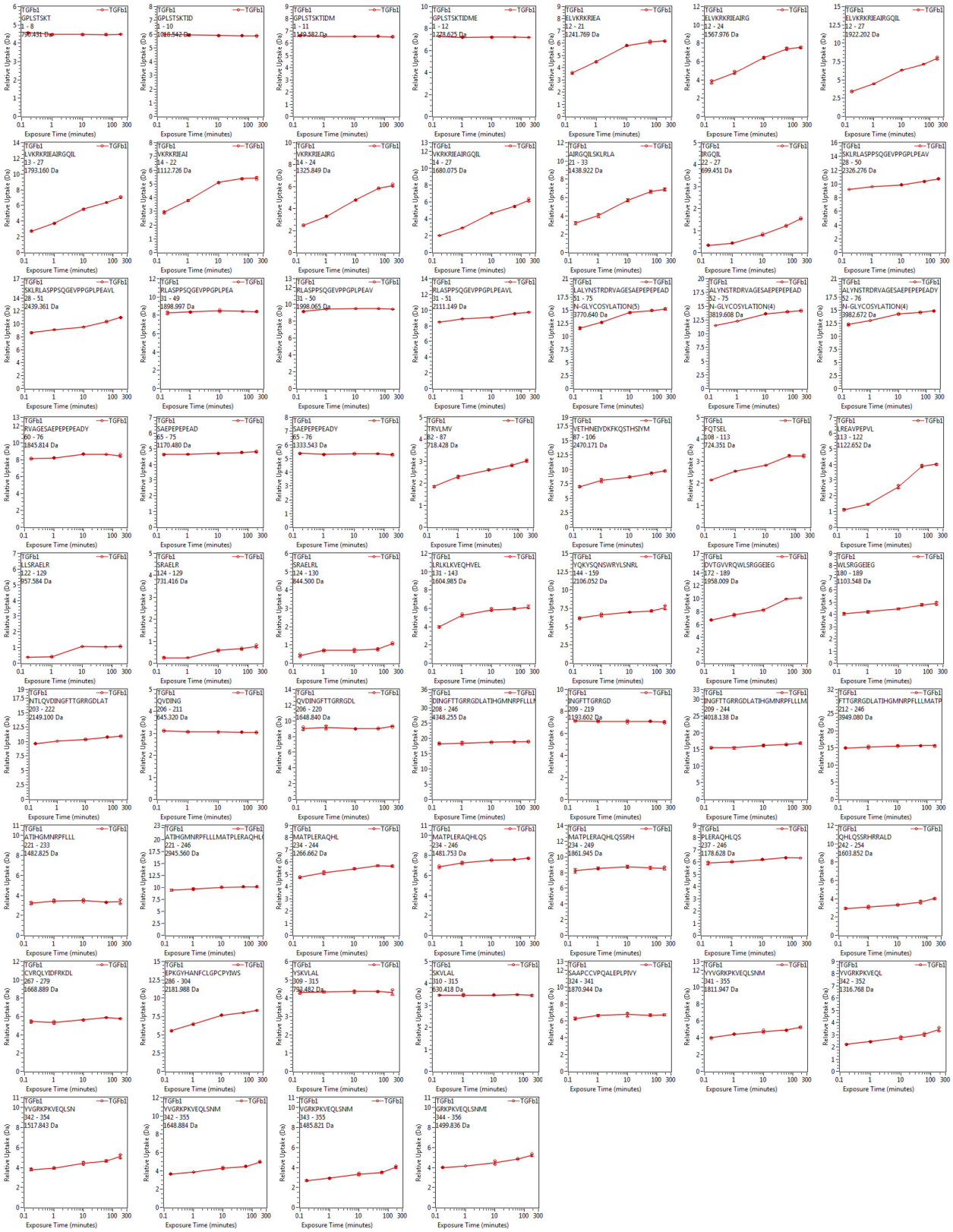

Extended Data Figure 4 | Deuterium incorporation kinetics for all peptic peptides followed with HDX-MS. Values represent the mean of three individual tests; error bars, s.d.

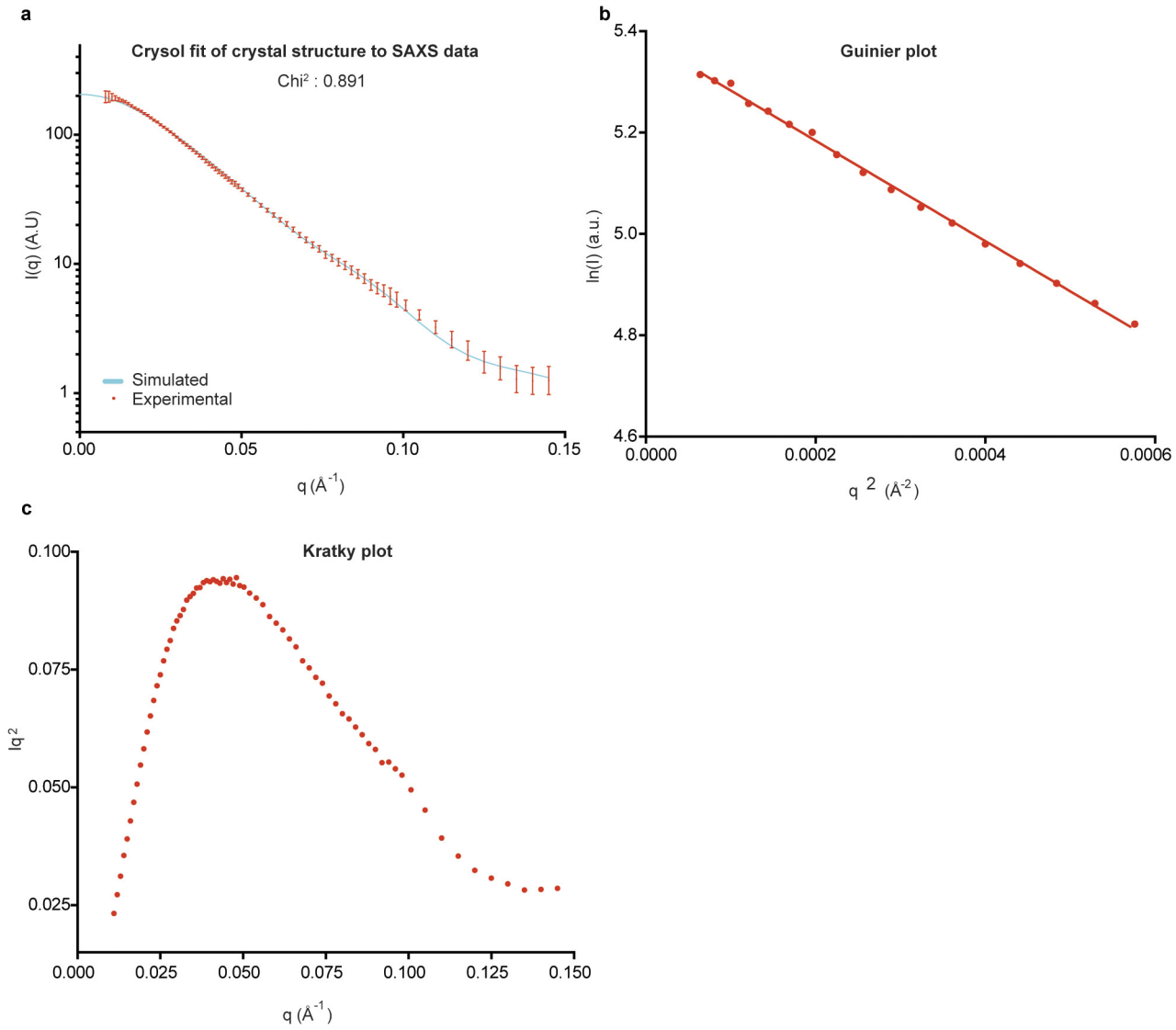

Extended Data Figure 5 | Validation of solution scattering of the 1:2 $\alpha_V\beta_6$/pro-TGF-β1 complex. Data are merged from samples at 0.4 and 3 mg ml^{-1}. **a**, Experimental SAXS of the 1:2 complex in solution (red, values represent mean and s.d of six datasets) versus the theoretical SAXS curve calculated with CRYSOL[26] from the crystal structure of the 1:2 complex (cyan). **b**, Guinier analysis of the merged data shows a linear fit in the low q region. **c**, The Kratky plot exhibits a typical bell-shaped peak.

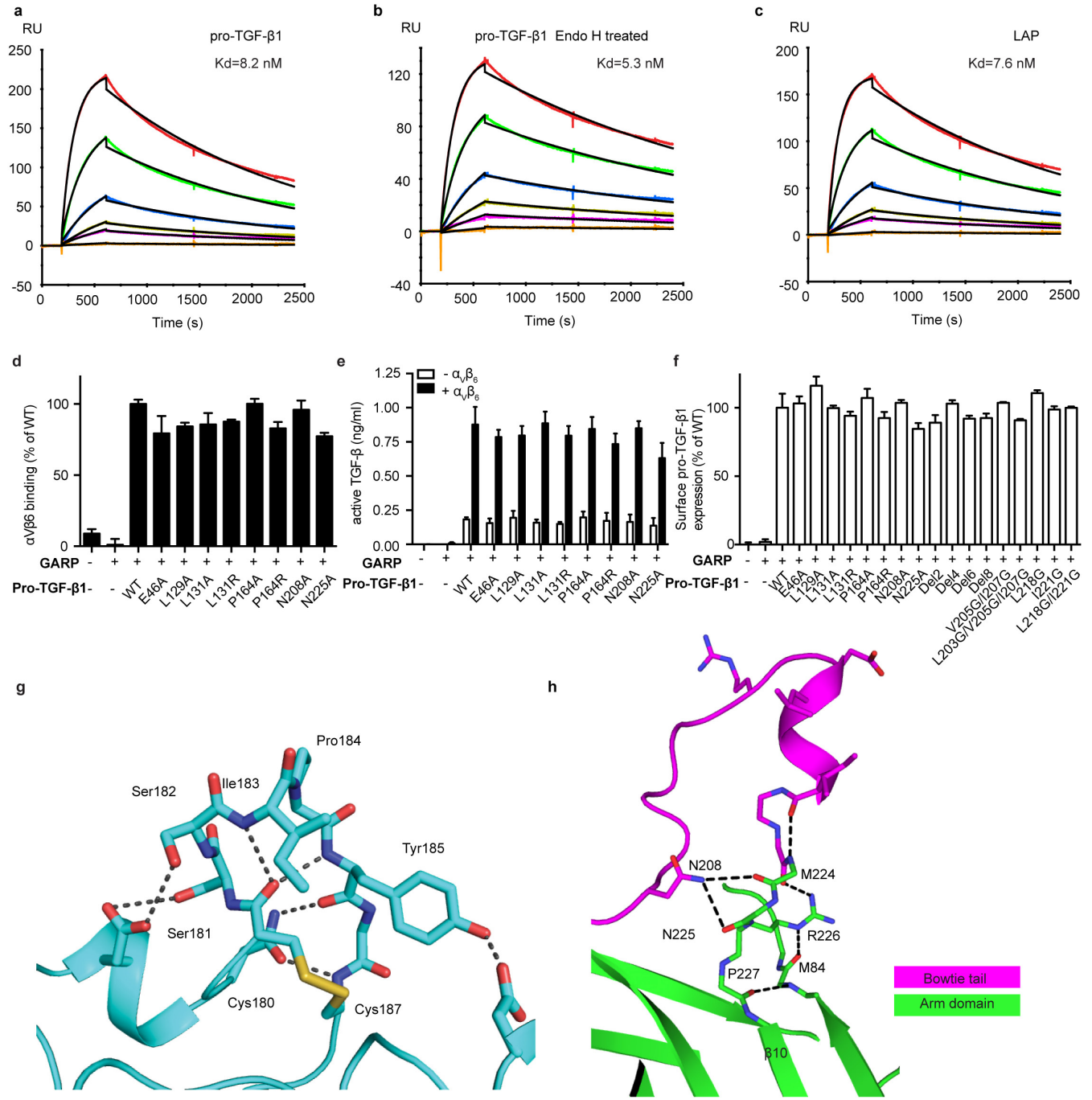

Extended Data Figure 6 | Binding, activation, and structural details. **a**–**c**, Surface plasmon resonance measurements of integrin $\alpha_V\beta_6$ headpiece binding to surface immobilized furin-mutant pro-TGF-β1 (**a**), endoglycosidase H (Endo H)-treated furin-mutant pro-TGF-β1 (**b**), and the untreated prodomain expressed in the absence of the growth factor (latency-associated peptide, LAP) (**c**). Curves are coloured red, 100 nM; dark green, 50 nM; blue, 20 nM; yellow, 10 nM; magenta, 5 nM; orange, 1 nM. The global fit to the 1:1 binding model is in black. Dissociation constant (K_d) and χ^2 values from fits are shown. **d**, Binding in presence of Mg^{2+} of FITC-$\alpha_V\beta_6$ to wild-type or mutant pro-TGF-β1/GARP HEK293T co-transfectants as specific mean fluorescence intensity (percentage of wild-type). The mutated residues lie on the arm domain outside the RGDLATI motif. **e**, Activation of TGF-β1 by HEK293T cells co-transfected with pro-TGF-β1 and GARP, with or without α_V and β_6, assayed with luciferase reporter cells, and standardized with purified TGF-β1. The mutated residues lie on the arm domain outside the RGDLATI motif. **f**, Expression of wild-type and mutant pro-TGF-β1/GARP complexes on 293T transfectants determined by immunofluorescence flow cytometry with TW7-28G11 antibody. Values represent the mean and s.d. of three independent transfections in **d**–**f**. **g**, Hydrogen bonds within SDL2 in the β_6 βI domain. **h**, The hydrogen bond network in the four residues, M224–P227, that link the bowtie tail to the β10 strand in the integrin-bound pro-TGF-β1 arm domain. Binding of integrin $\alpha_V\beta_6$ to pro-TGF-β1 does not liberate the growth factor[3]. The experiments in **a**–**c** address the question of whether integrin binding loosens the grip of the prodomain on the growth factor. Destabilization of the binding energy for the growth factor would require an identical stabilization of integrin binding to the isolated prodomain compared with the pro-complex; however, this is ruled out by the equivalent dissociation constants for integrin $\alpha_V\beta_6$ binding to the prodomain (7.6 nM, **c**) and pro-complex (8.2 nM, **a**). Thus, in the absence of force, there is no propagation of conformational change from the integrin binding site to the prodomain/GF interface that lowers affinity for ligand. The β_6 SDL2 backbone is supported by many backbone hydrogen bonds (**g**), correlating with the finding that, in the open β_6 conformation determined here, SDL2 is essentially identical in backbone to the previous closed conformation bound to the TGF-β3 peptide[4]. In contrast, SDL2 in β_2 moves, even in intermediate headpiece opening[17].

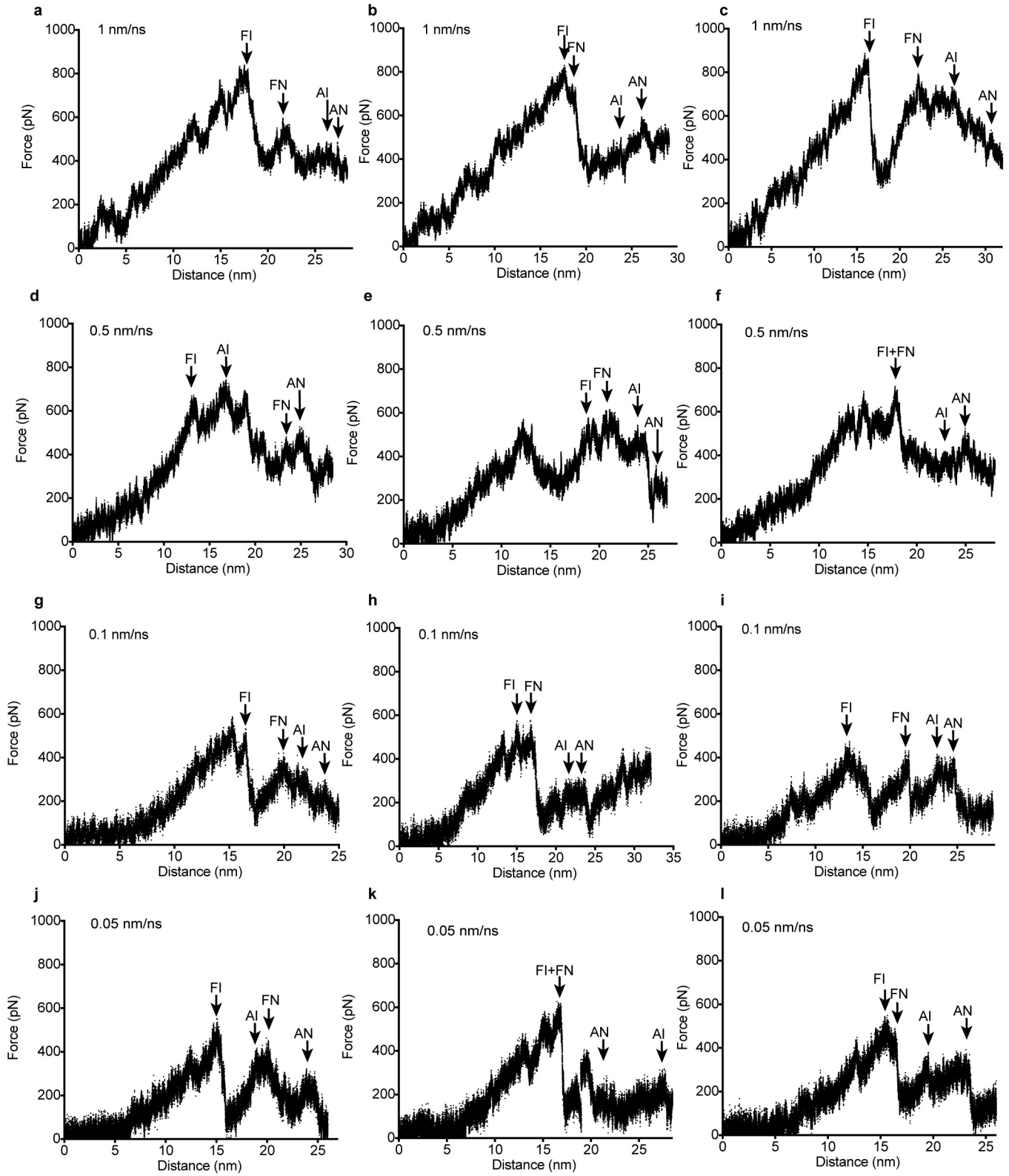

Extended Data Figure 7 | Force spectroscopy in β_6 pulling simulations. **a**–**l**, Force on the harmonic spring at the pulling end was measured every picometre in independent simulations at the indicated pulling rates. The four major events in straitjacket removal are arrowed in each simulation with two-letter codes. The first letter is F for fastener unsnapping and A for α2 helix unfolding. The second letter is I for the integrin-bound monomer and N for the non-bound monomer.

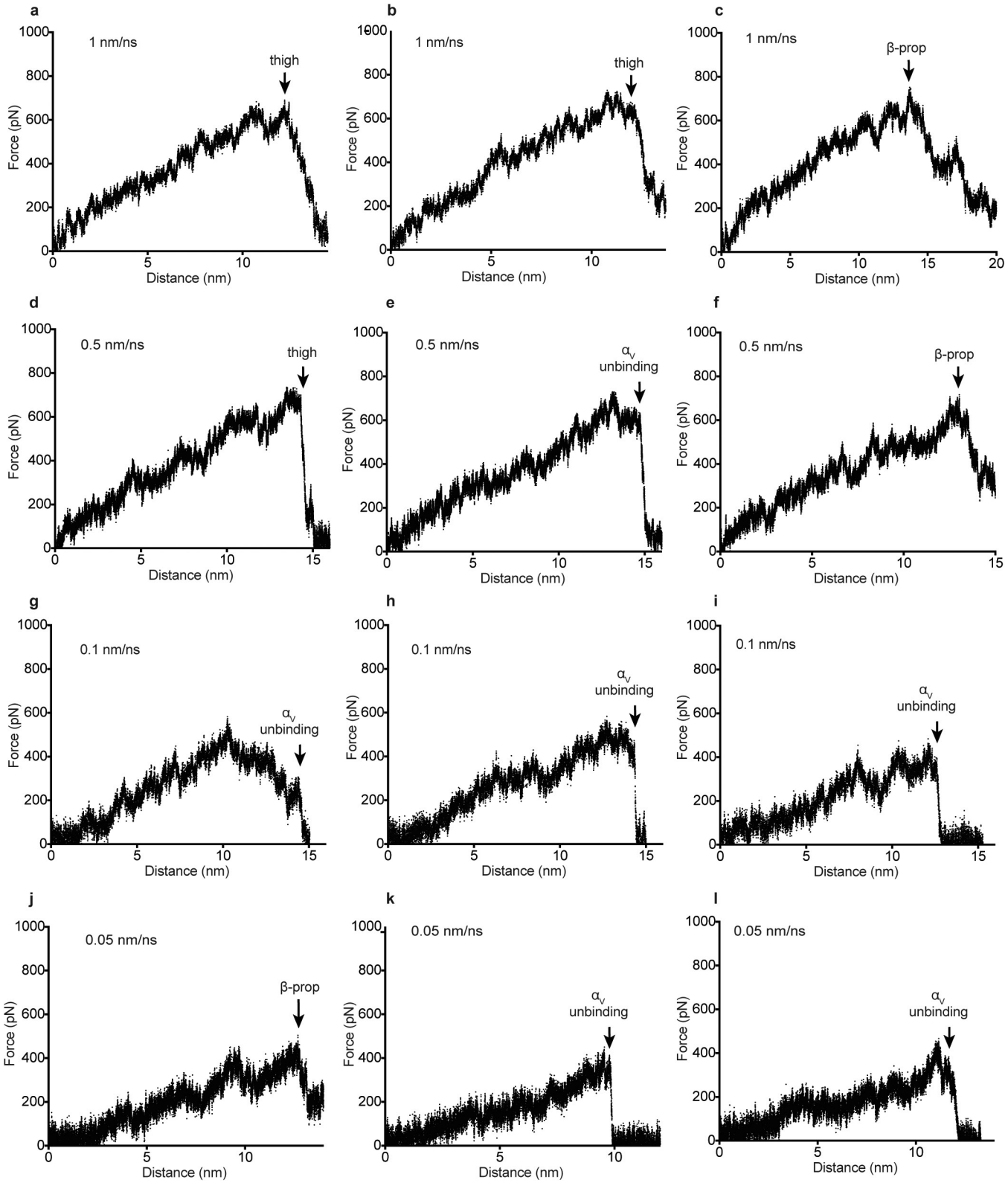

Extended Data Figure 8 | Force spectroscopy in α_V pulling simulations. **a–l**, Force on the harmonic spring at the pulling end was measured every picometre in independent simulations at the indicated pulling rates. Pulling failed in each simulation (arrows) owing to thigh domain unfolding (thigh), β-propeller domain unfolding (β-prop) and separation of the α_V β-propeller domain from pro-TGF-β1 and the β_6 βI domain (α_V unbinding).

Extended Data Table 1 | Data collection and refinement statistics

	$\alpha_V\beta_6$ head (5FFG)	$\alpha_V\beta_6$ head/ proTGF-β1 (5FFO)
Data collection		
Space group	C2	P1
Cell dimensions		
a, *b*, *c* (Å)	215.6, 77.6, 59.1	81.4, 91.4, 131.0
α, *β*, *γ* (°)	90, 101.5, 90	90.0, 86.3, 89.9
Resolution (Å)	50.0-2.20(2.26-2.20) [a]	50.0-3.50 (3.64-3.50)
R_{merge}	6.5 (63.3)	16.8 (178.8)
$I/\sigma(I)$	6.7 (1.3)	4.6 (0.4)
$CC_{1/2}$	99.5 (60.6)	98.8 (12.4)
Completeness (%)	94.7 (98.9)	94.6 (97.1)
Redundancy	2.4 (2.3)	1.8 (1.8)
Refinement		
Resolution (Å)	50.0-2.20	50.0-3.50
No. reflections	90,185 (6,922)	45,279 (3,450)
R_{work} / R_{free}	20.6(33.3)/24.9(38.6)	23.2 (30.2)/27.9 (33.9)
No. atoms		
Protein	6492	22945
Ligand/ion	337	836
(Carbohydrate/Metal ion)		
Water	243	5
B factors		
Protein	60.5	216.70
Ligand/ion	90.0	248.40
Water	53.4	142.30
R.m.s. deviations		
Bond lengths (Å)	0.005	0.007
Bond angles (°)	0.7	0.8

One crystal dataset was collected for each structure. Values in parentheses are for highest-resolution shell.